Uncovering temperature-tempted coordination of inclusions within ultra-high-strength-steel via in-situ spectro-microscopy

Rani, Ekta

2022-03-01

Rani , E , Singh , H , Alatarvas , T , Kharbach , M , Cao , W , Sarpi , B , Zhu , L , Niu , Y , Zakharov , A , Fabritius , T & Huttula , M 2022 , ' Uncovering temperature-tempted coordination of inclusions within ultra-high-strength-steel via in-situ spectro-microscopy ' , Journal of Materials Research and Technology , vol. 17 , pp. 2333-2342 . https://doi.org/10.1016/j.jmrt.2022.01.170

http://hdl.handle.net/10138/344400
https://doi.org/10.1016/j.jmrt.2022.01.170

JOURNAL OF MATERIALS RESEARCH AND TECHNOLOGY 2022;17:2333–2342

Available online at www.sciencedirect.com

jmr&t Journal of Materials Research and Technology

journal homepage: www.elsevier.com/locate/jmrt

Original Article

Uncovering temperature-tempted coordination of inclusions within ultra-high-strength-steel via in-situ spectro-microscopy

Ekta Rani [a], *Harishchandra Singh* [a,b,*], *Tuomas Alatarvas* [b,c], *Mourad Kharbach* [a], *Wei Cao* [a,b], *Brice Sarpi* [d], *Lin Zhu* [d], *Yuran Niu* [d], *Alexei Zakharov* [d], *Timo Fabritius* [b,c], *Marko Huttula* [a,b]

[a] *Nano and Molecular Systems Research Unit, University of Oulu, FIN-90014, Finland*
[b] *Centre for Advanced Steels Research, University of Oulu, FIN-90014, Finland*
[c] *Process Metallurgy Research Unit, University of Oulu, FIN-90014, Finland*
[d] *MAX IV Laboratory, Lund University, Lund, 22484, Sweden*

ARTICLE INFO

Article history:
Received 8 November 2021
Accepted 31 January 2022
Available online 7 February 2022

Keywords:
Low carbon steel
X-ray synchrotron radiation
In-situ
X-ray absorption spectroscopy
Non-metallic inclusion

ABSTRACT

Despite the common challenge of investigating non-metallic inclusions within ultra-high-strength-steel (UHSS) at sub-micrometer scale via conventional methods, probing nitride inclusions at elevated temperatures is vital for guiding steel' performance. Herein, an in-situ spectro-microscopic determination using advanced Synchrotron X-ray absorption spectroscopy (XAS) coupled with photoelectron emission microscopy (PEEM) is employed to explore the local structure and electronic properties of selective h-boron nitride (h-BN) containing inclusions (A1 and A2) embedded within steel matrix. While the variation in the relative intensity of π^*/σ^* excitonic peaks at spatially different locations refers to the polarization and or thickness effects. Several minute features observed in the 192–195 eV energy range show oxygen (O) substituted nitrogen (N) defects ($O_{N,2N,3N}$), which are more dominant in A2 inclusion. The observed dominance further explains the relatively high intense π^* peak in A2 due to increased localization. Weak shoulder on the left side of π^* peak in both room and high-temperature XAS spectra is ascribed to the interaction between h-BN and the local environment, such as Ca-based inclusion or steel matrix. Defects are commonly found in h-BN, and precise identification of the same is vital as they affect the overall physical, chemical, and mechanical properties. Moreover, significant changes in high-temperature B K-edge XAS spectra, such as relative intensity of π^*/σ^* excitonic peaks at the same location and reduced intensity of defects, suggest the adjusting nature of BN inclusion, complicating their precise prediction and control towards clean steel production.

* Corresponding author.
E-mail address: Harishchandra.Singh@oulu.fi (H. Singh).
https://doi.org/10.1016/j.jmrt.2022.01.170

1. Introduction

The high mechanical strength of ultra-high-strength-steel (UHSS), achieved with thermomechanical treatments post-casting, enables lighter constructions with compact design, which further effectively controls global warming [1,2]. Although adequate emphasis has constantly been given to the UHSS's microstructure to attain its far-reaching performance, the influence of non-metallic inclusions (NMIs) on its properties is comparatively unnoticed and left to researchers interested in the comprehensive studies. In contrast, the importance of NMIs in the steel making and their performance has been persuasive in the industry for decades. NMIs are non-metallic chemical compounds, such as sulfides (CaS, MnS), oxides, such as spinel ($MgAl_2O_4$) and calcium aluminates ($xCaO.yAl_2O_3$), and nitrides (AlN, BN, TiN) within the steel matrix, formed during the different stages of steel production [3]. Inclusions can significantly affect the microstructure and properties of the final steel product [3]. For example, coherent phases, such as precipitates, may enhance the overall performance of steel, whereas incoherent NMIs can have a more detrimental effect. Thus, tailoring inclusions to improve properties has been a central feature of the steel-making industry and was termed "inclusion engineering" in the 1980s [4], which requires an in-depth understanding of the relationship between the type, size, and distribution NMIs with the steel matrix. Furthermore, it is imperative to study the behaviors of these NMIs during various processing conditions, which are employed to enhance steel properties. Thus, although the comprehensive mechanistic studies of NMIs' formation and their interaction within and with steel matrix are scarcely reported but crucial as different alternatives, such as graphene, have additionally challenged steel.

Among the possible variety of inclusions observed, the chemical composition of commonly formed oxide and sulfide inclusions is associated with the total composition of the steel, including oxygen and sulfur. On the other hand, nitrides (i.e., nitrogen-based NMIs) are often overlooked since they form during solidification and usually are not among the largest NMIs [5]. Nevertheless, steel contains some nitrogen, which can enter the steel matrix as an impurity or an intentional alloying addition, giving rise to various nitride inclusions, such as TiN and BN [5]. Various non-destructive microscopic determinations and elemental specifications have already been employed to study NMIs [6–9]. Moreover, partially destructive electrolytic extraction to dissolve the steel matrix around an inclusion followed by imaging has been performed [10]. Conventional methods, however, fail to provide chemical information of such NMIs at the sub-micrometer level. Thus, determining the coordination chemistry and chemical components of such inclusions is challenging, wherein destructive methods are ruining the inclusions. Complications with chemical separations at the sub-micrometer scale within inclusions are another concern. Thus, a spectro-microscopic method with chemical sensitivity and good lateral resolution [11,12] is vital for studying the local manipulation of NMIs embedded within the steel matrix, especially during various processing conditions. Recently, we employed non-destructive room temperature (RT) X-ray absorption (XAS)-photoelectron emission microscopy (PEEM), referred to as X-PEEM [13], to study several selective NMIs. X-PEEM is a spectro-microscopic full-field, synchrotron-based surface-sensitive technique that relies on the availability of a tunable and brilliant X-ray source. The high sensitivity of the XAS spectrum to the chemical composition, phase, and the local environment makes X-PEEM a highly attractive technique. Changes in the XAS spectrum at the spatially different position can be monitored further to offer simultaneous microscopy and spectroscopy. Furthermore, the in-situ XAS spectrum can probe the same features, e.g., oxidization states, local structure, and electronic structure of selected elements.

This work focuses on the temperature-dependent in-situ X-PEEM investigation of two BN inclusions within UHSS. Nitrides are known to control the grain size evolution during thermomechanical treatments. Interestingly, although BN is not expected in such UHSS, they can form during the steel solidification process or secondary phases. In general, these inclusions are usually small in size and thus, are not expected to worsen the properties of steel. Nevertheless, so far, to our best knowledge, there are no reports on the in-situ evolution of the BN inclusion within the steel matrix at elevated temperatures using the XAS. This work presents the first systematic in-situ spectro-microscopic manipulation and monitoring of BN inclusions within a typical carbon steel matrix to elucidate their formation and interaction mechanism with other inclusions and the steel matrix.

2. Experimental section

The selected steel sample is commercial low-alloyed carbon steel [13] with a nominal composition of 0.15C, 0.3Si, 1.0Mn, 0.4Cr in wt.%. The microstructural phases were recorded via high-energy synchrotron X-ray diffraction and discussed in the previous work [13]. Field emission scanning electron microscopy-energy dispersive spectroscopy (FESEM-EDS) was employed to carry out the morphological and elemental determination via FESEM Zeiss Ultra Plus. For the present in-situ spectro-microscopic determination, two dedicated nitride inclusions (i.e., A1 and A2) containing BN have been selected and probed at different temperatures. The X-PEEM measurements on these two selected model systems were carried out at the AC-SPELEEM end-station of MAXPEEM Beamline at MAX IV laboratory (Lund, Sweden), using a modified SX-700 monochromator equipped with 300 lines.mm^{-1} (low-density) or 1220.9 lines.mm^{-1} (high-density) Au/Si grating. The beamline energy bandwidth was estimated to be 2×10^{-4} with a photon flux of $1–5 \times 10^{12}$ ph s^{-1} (200–900 eV range). All samples were degassed in an ultrahigh vacuum preparation chamber prior to exposure to synchrotron radiation. The photon energy was scanned across B K-absorption edge with a 0.2 eV step. An X-PEEM image was recorded at each energy with a TVIPS F-216 optical fiber-coupled CMOS detector with 2×2 binning, which provides 1024×1024 pixels in the 30 μm field of view. The exposure time was set to 0.2 s with an averaging number of 16 frames. The spatially resolved XAS spectra were collected in partial yield at the energy of the

highest secondary photoelectron signal, comparable with total electron yield mode. The energy dispersion was narrowed down to 0.5 eV using a slit inserted at the exit of the energy analyzer to improve spatial resolution. All measurements were carried out using linearly polarized X-rays in conditions of normal incidence relative to the sample surface. The high temperature (HT) data were collected in real-time from samples annealed under ultra-high vacuum at 400 °C via resistive heating of a filament inside the sample holder. The temperature was monitored by means of a thermocouple positioned at the rear face of the sample. More details regarding the PEEM measurements can be found in the previous studies [12,14,15].

The behavior of BN inclusions was further studied by building the spatial distribution maps (chemical signal images) towards a reliable interpretation of the maximum energy absorption under two conditions (RT and 400 °C). The benefit of this approach is to provide the quantitative elemental information, chemical shift, location, and nature of inclusions. Moreover, these maps exhibited the local variation within the inclusions, wherein the relative intensity variation of π*/σ* resonance was highlighted. The resulting chemical images were displayed in false colors, where the color contrast represented different X-ray absorption and the change in inclusion content is assigned with a linear color scale. The distribution images were obtained by averaging signal spectra at the individual pixels in the energy range of 191.4–194.0 eV (π* resonance) and 196.4–201.6 eV (σ* resonance) to extract the highest energy absorption (intensity). The false color pixel classification is a spatially resolved spectra from a 200 × 200 pixels field of view.

3. Results

Fig. S1 depicts SEM images of two NMIs embedded in the steel matrix. As per the elemental composition analysis ([13] and Table 1), the selected A1 and A2 inclusions contain mainly Ca-based compounds, whereas the presence of B-based compounds and their interaction with local environments was not clear. To get insight in the formation of BN inclusion, the B element is investigated with chemical distinctions at micro-regions. The analysis also includes calibrations with the published data, for example, B K-edge [16].

Table 1 – EDS point analyses for the selected regions of two inclusions. These compositions are shown in the wt%.

Elements	A1			A2			
	2	3	4	6	7	8	9
B					36.19	29.23	34.98
N					23.16	19.08	16.67
O	22.59	13.59	11.52	24.63	2.06	1.55	
Mg				3.25	0.10		
Al	3.46	0.40	0.51	9.42	1.03	0.29	0.11
Si	0.25	0.56	0.82			0.13	
S	22.03	2.59	1.57	16.54	1.24	0.50	0.13
Cl							
Ca	34.28	2.82	1.76	27.31	2.44	0.74	0.18
Ti	0.59	0.07	0.13	0.50			
Cr	0.37	1.13	1.26			0.31	0.31
Mn	0.17	0.87	0.71		0.38	0.36	0.98
Fe	16.26	77.97	81.71	18.35	33.39	47.82	46.64

3.1. Room temperature spectro-microscopic determination

X-PEEM image and corresponding B K-edge XAS spectra for A1 and A2 inclusions are depicted in Figs. 1 and 2. Three significant features are resolved at the B K-edge XAS spectra, numbered b1, b2, and b3. Feature b1 (~192 eV) is the well-known π* ($2p_z$) resonance of h-BN. Higher energy features b2 and b3 are assigned to σ* resonance of h-BN. Although the σ* doublet feature is consistently observed in bulk, monolayer, and or h-BN nanotubes, there is debate over its origin [16–18]. For example, theoretical calculations suggest a single σ* peak in pristine BN, whereas the asymmetric/doublet σ* peak is created by boron vacancies (V_B) passivated by H atoms [18]. On the other hand, as per the molecular orbital perspective, the intense double feature ~198.2 eV and ~ 199.6 eV is assigned to the localized σ* ($2p_x$, $2p_y$) antibonding between B and N or as per the band theory, they have been attributed to the transitions to the maximum density of states at the L/M and Γ point of the first Brillouin zone of h-BN, respectively [19]. Figure 1 further shows B K-edge XAS spectra at different spatial locations within the chosen inclusion. Comparative studies show variation in intensity relation of π* and σ* peak at different locations. It is known that h-BN nanosheets are highly polarized. Additionally, a highly flat h-BN nanosheet should

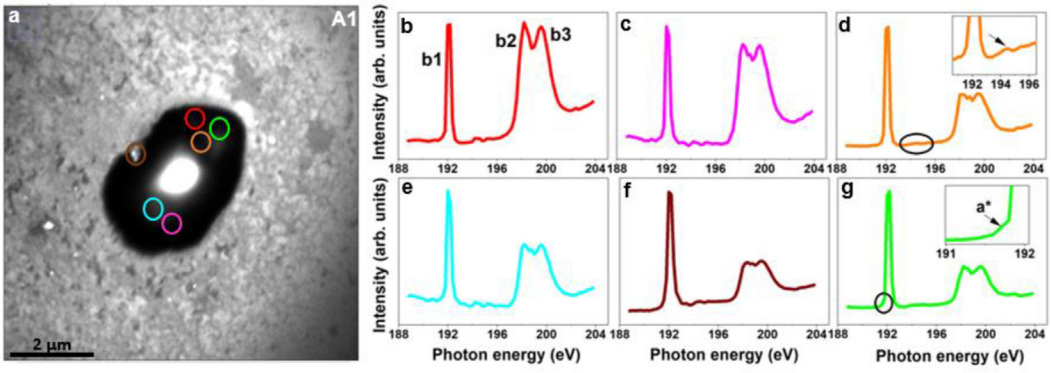

Fig. 1 – X-PEEM image (a) and corresponding XAS spectra (b–g) at selected locations (marked with circles) for A1 inclusion.

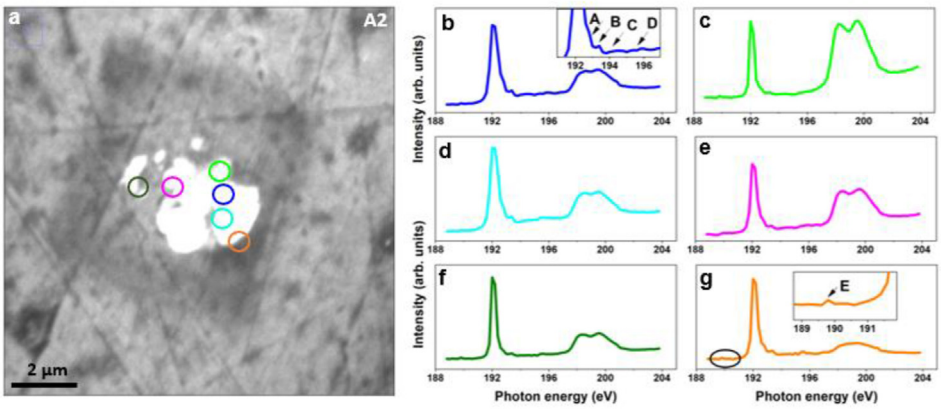

Fig. 2 – X-PEEM image (a) and corresponding XAS spectra (b–g) at selected locations (marked with circles) for A2 inclusion.

have a negligible π* peak for spectra acquired with the normal beam incidence as the in-plane linearly polarized X-ray beam's electric vector is orthogonal to it and thus, cannot excite the π* resonance [16]. The weakly visible π* have been proposed to arise from wrinkle/folding of the sheets, the lower crystallinity of surface domains/islands, and/or a slight misalignment of the sample with respect to the incident beam. Whereas the sample tilted at 30° with respect to the incident beam gives a strikingly high-intensity π* peak [16]. In the present case, wherein normal incidence is employed, the intensity of π* is either greater or comparable to that of the σ* peak. This suggests that higher intensity π* peak observance could also be assigned to the polarization effect, indicating that h-BN sheets are not flat and tilted at different angles. Furthermore, as per the previous reported work [16], a systematic TEM and XANES measurements suggest that variation in the number of layers of h-BN, such as single layer or different multilayered h-BN show variation in the relative intensity of π*/σ* peak, whether it is normal incidence or the sample is tilted at 30° with respect to the incident beam. This suggests that there can be a possibility of h-BN sheets grown with different number of layers at spatially different locations, that is, the thickness effect, cannot be entirely ignored. Similar features have been noted for another chosen inclusion, A2 (Fig. 2). However, comparison of the relative intensity of π* and σ* peaks suggests that mainly higher intensity π* peak has been found. This indicates that polarization and/or thickness effect may not be the sole factor behind the observance of higher intensity π* peak as both inclusions are observed in the same steel matrix, processed under the same experimental conditions.

Apart from the dominant peaks, other minute but significant features are also noted in XAS spectra in the vicinity of the 1s to π* peak on the high-energy side, which are not observed for pristine h-BN [18,20]. As per literature, various minute features have been recognized as different point defects, such as B vacancy (V_B), N vacancy (V_N), C substituted for B (C_B), C substituted for N (C_N), O substituted for B (O_B), and O substituted for N (O_N) in h-BN. Herein, a weak contaminant feature at ~194.4 eV (denoted as C) and another feature at ~196 eV (denoted as D) hardly distinguishable from the noisy background are noted at specific locations in A1 (Fig. 1d). A2 inclusion, on the other hand, displayed peaks located at ~192.8 eV (denoted as A), ~193.3 eV (denoted as B), ~194.4 eV (C), and ~196 eV (D) (Fig. 2b). Observed small features in the B K edge π* peak region (191–195 eV) have been understood to be related to O association [18,21]. Moreover, multiple features in this region have been attributed to multiple substitutional O defects with the probability of stable triangular defects with O-terminated edges in h-BN, that is, a varied local bonding environment [21]. Furthermore, the relative intensity of this triplet feature with respect to the main π* peak has been found to be correlated with the O content of the film. Therefore, these features have been hypothesized as satellite peaks originating from B atoms whose local BN_3 coordination is altered by the substitution of up to three N atoms with O atoms, where the highest energy peak (194.4 eV) corresponds to a B coordinated to three O atoms substituted at three N sites (O_{3N}), which is also in corroboration with the theoretical XAS calculations at near edge [21]. Thus, these three features at 192.8, 193.3, and 194.4 eV can be attributed to excitations from B atoms to regions that have BN_2O (O_N), BNO_2 (O_{2N}), and BO_3 environments. The observed feature at ~196 eV has been attributed to surface contaminants and defects, pronounced in the single-layer h-BN followed by a gradual decrement in the intensity with increasing layer number [16]. This observation further suggests the presence of different layers of h-BN in the inclusions.

The above proposition of varied O environment can further explain the observance of mainly higher intensity π* peak (compared to σ* peak) in A2 inclusion accompanied with these three peaks (Fig. 2), whereas relative lower intense π* peak (compared to σ* peak) in A1 inclusion is accompanied with mainly one peak. As per XAS calculations [21], the characteristics of the excitonic state do not change with the change in the local O coordination of the excited boron atom and remain a highly localized state with antibonding p orbital. The electron density is mainly localized on the excited atom and its first and second nearest neighbor atom N. The introduction of O atoms breaks these B–N bonds leading to enhanced localization of the excitonic state on the remaining bonds. This increased localization further increases the overlap with the

Table 2 – XAS spectral features and their possible origin.

Peak termed as	Spectral feature (~eV)	Origin
b1	192	π^* ($2p_z$) resonance
b2	198.2	σ^* ($2p_x$)
b3	199.6	σ^* ($2p_y$)
A	192.8	BN_2O (O_N),
B	193.3	BNO_2 (O_{2N})
C	194.4	BO_3 (O_{3N})
D	196	surface contaminants and defects
E	189.8	C_N
a*	191.4	Hybridization between 3d-states (transition metal) and π band (h-BN) or in–gap metallic state

1s core state, giving rise to increased intensity of the π^* feature with the increment in O coordination, apart from the polarization and thickness effect noted above.

The another observed weak shoulder (Fig. 1g) on the left side of π^* peak can be assigned to 1s to mid-gap states induced by 3d-states (transition metal) and π band (h-BN) hybridization [17,22] or in–gap metallic states [23], indicating the interaction between h-BN inclusion and the environment, which can be Ca-based inclusion or steel. This further agrees with our recently published work showing that h-BN inclusion is only stabilized with Ca-based inclusions [13].

Another observed minor feature at ~189.8 eV (Fig. 2g) can be attributed to C substitutional defect structures [18]. C substitution at B or N site can modify the adjoining bond lengths while maintaining the D_{3h} threefold symmetry. The C_B defect produces π^* peak shifts to higher energy along with splitting, while the main σ^* peak has higher energy and a shoulder. H passivation of C_B (C_{B-H}) results in the B K edge π^* peak shifted to higher energy without splitting. On the other hand, C_N causes pre-edge features in the B K-edge as observed in the current inclusions, indicating the presence of unoccupied states in the bandgap, which are filled upon H passivation (C_{N-H}). Thus, the experimental feature at ~189.8 eV can be attributed to C_N defect (Fig. S3).

All the spectral features are tabulated in Table 2. In short, among the various point defect generally observed in h-BN in these inclusions, O_N, O_{2N}, O_{3N}, and C_N seem to be dominated. Furthermore, O-terminated defects with the substitution of up to three N atoms are found to be significantly more stable than defects with N-terminated edges. To study the BN inclusion's behavior with temperature, we further carried out in-situ spectro-microscopic investigations in conditions comparable to tempering stage of steel.

3.2. *High temperature in situ spectro-microscopic determination*

Figures 3 and 4 and Fig. S3, S4 display the comparative X-PEEM thermal image (Figs. 3a,b and 4a,b) and corresponding B K-edge

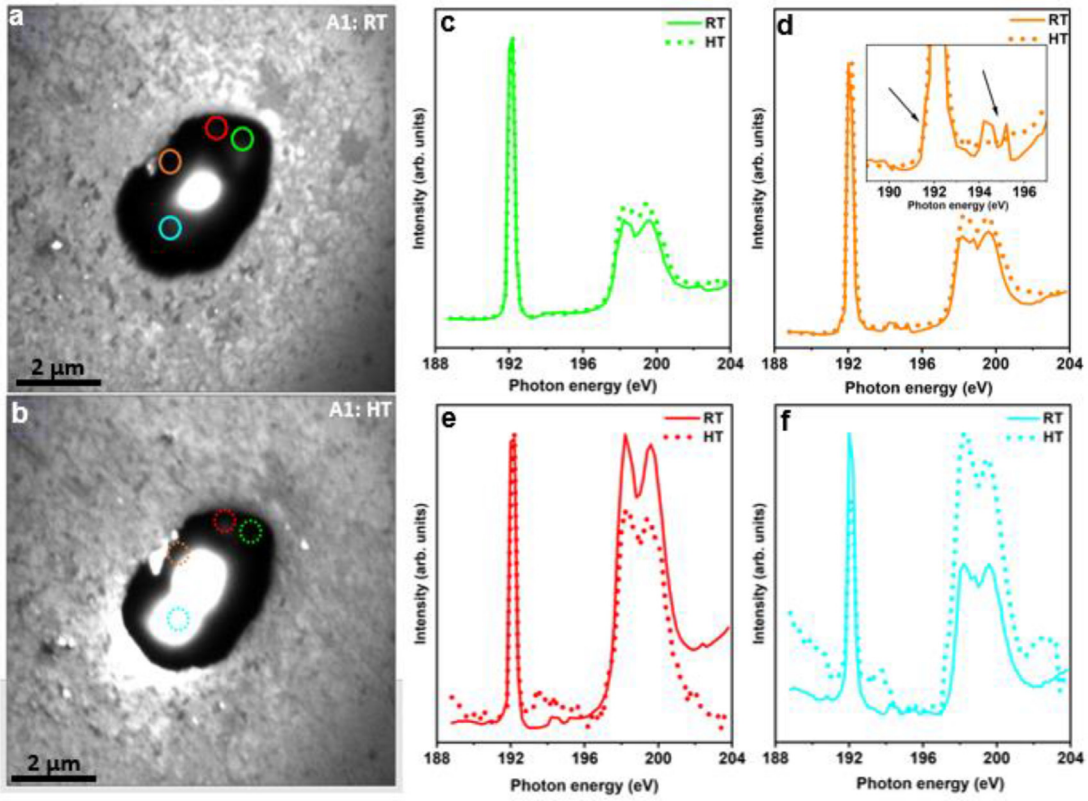

Fig. 3 – Comparison of RT (a) and HT (b: 400 °C) annealed X-PEEM image and corresponding XAS spectra (c–f) at selected locations (marked with circles) for A1 inclusion along with changes in the minute features as shown in inset of Fig. 3d. Solid line and dotted line represent spectra for RT and HT, respectively.

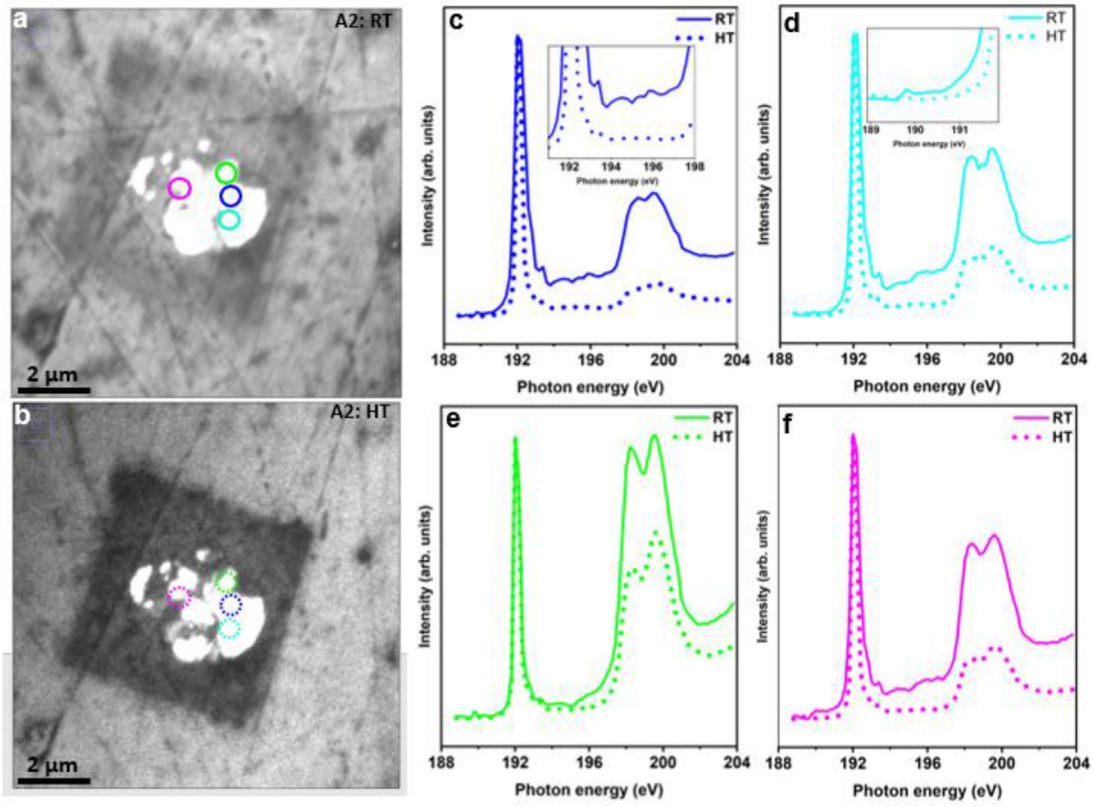

Fig. 4 – Comparison of RT (a) and HT (b: 400 °C) annealed X-PEEM image and corresponding XAS spectra (c–f) at selected locations (marked with circles) for A2 inclusion along with changes in the minute features as shown in inset of Fig. 4c & 4d. Solid line and dotted line represent spectra for RT and HT, respectively.

XAS spectra (Figs. 3c-f and 4c-f) at marked positions for A1 and A2 inclusions, measured at RT and 400 °C. Significant changes have been noted for XAS spectra collected at 400 °C, such as i) change in the relative intensity of π*/σ* peak at the same location, ii) varied intensity of weak shoulder on the left side of π* peak at certain locations, and iii) reduced intensity of peaks A-D located at 192.8193.3, 194.4 and 196 eV in the vicinity of 1s to π* peak (Figs. 3d and 4c). Change in the relative intensity of π*/σ* peak at the same location can be assigned to adjusting nature of BN inclusion within the A1 and A2 inclusions. This is evident from the X-PEEM thermal images (Figs. 3 and 4). Following annealing in the vacuum, intensities of peaks A-D decrease. This further supports the O association of these peaks as proposed in the RT XAS data. This indicates that peaks A–D originate from in-plane defects, which get reduced on vacuum annealing. These results further emphasize that peaks A, B, and C are associated with O substituted at N atom, two N sites, and three N sites, respectively. The observed weak shoulder on the left side of π* peak even after vacuum annealing (Fig. 4d) further support that it does not arise from O-defects and indeed can be assigned to 1s to mid-gap states induced by 3d–π orbital mixing [17] or in–gap metallic states [23], indicating the interaction between h-BN inclusion and the local environment, which can be Ca-based inclusion or steel. Thus, the observed C_N defect in RT XAS spectra seems to have reduced intensity in the vacuum annealed XAS spectra. Vacuum annealing has, thus, led to the reduction in defects in the BN inclusion.

3.3. *Chemical distribution maps for inclusion A1 and A2*

The changes in the image intensity between RT and 400 °C for the A1 inclusion are displayed in Fig. 5. The π* peak is obviously decreased by 5 folds (Fig. 5a & c) and decreased by 3 folds for σ* peak (Fig. 5b & d). On the other hand, for the A2 inclusion (Fig. 6), the changes in the image intensity of π* peak is noticeably reduced by 3 times (Fig. 6a & c), and by 4 times for σ* peak (Fig. 6b & d) between RT and 400 °C, respectively. Particularly, the change is also remarked in the ratio of relative intensity of π*/σ* for the two inclusions A1 and A2, and regarding the signal-to-noise ratio. Thus, chemical distribution maps clearly emphasize the drastic variation in the energy intensity under annealing at 400 °C.

4. Discussion

4.1. *Formation of h-BN*

B is used as a microalloying element in high-strength steels to improve hardenability. Therefore, the formation of BN is not encouraged, and to prevent it, one solution is to carry out titanium alloying to protect additional boron [24]. The formation of TiN is preferred over BN to maintain boron in the steel matrix. BN occurs in two main crystalline phases, cubic BN (c-BN) and hexagonal BN (h-BN). It is known that BN is very difficult to

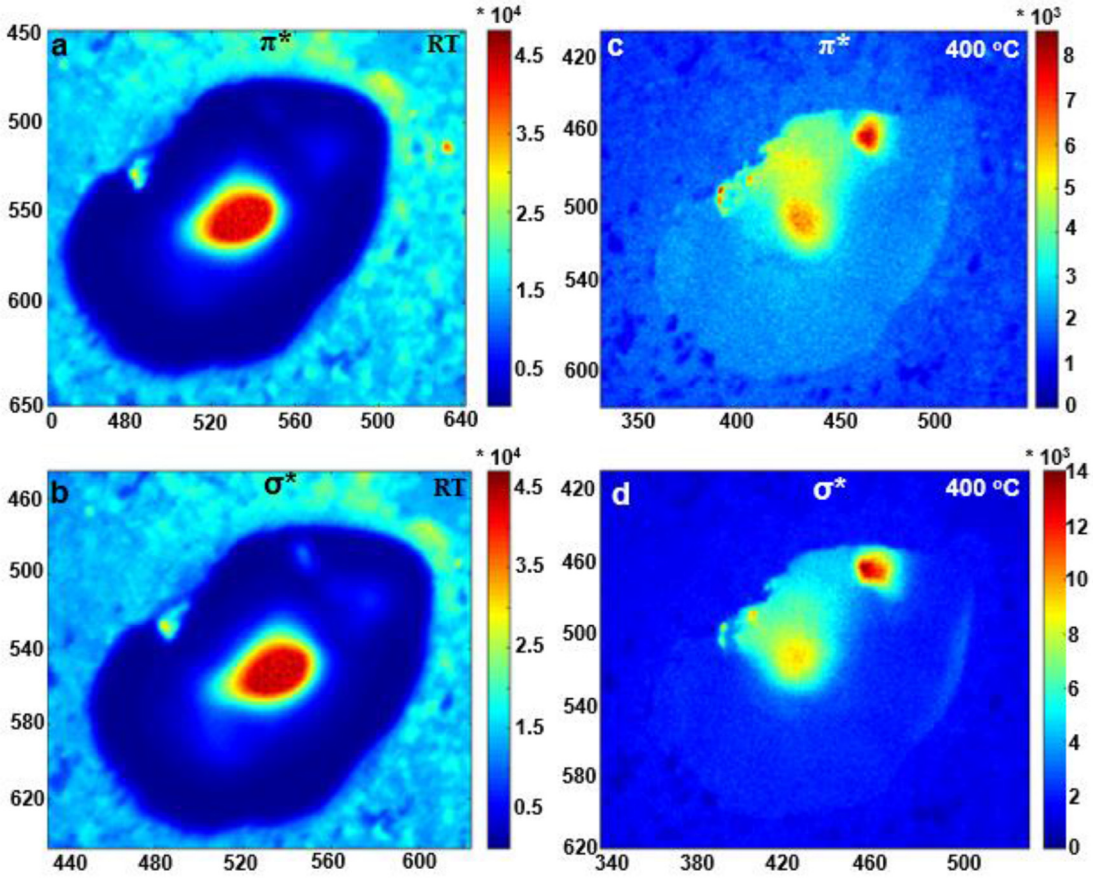

Fig. 5 – False color distribution maps displaying the maximum energy absorption in the local spatial variation in the 200 × 200 pixels field of view for inclusion A1 at RT (a & b) and 400 °C (c & d), Top to bottom, pixels colored with the intensity (number of counts) shown at one pixel as a function of energy. Contrast and quantitative image analysis were distributed between blue color (lowest absorption) and red (highest absorption).

synthesize in the cubic phase, whereas the formation of h-BN is relatively easy. h-BN possesses a graphite-like structure consisting of strong B–N covalent bonds forming sp^2 bonded hexagons (Fig. 7), with weak bonding between consecutive layers. Moreover, defects are commonly found in h-BN in the general field of material science, and precise identification of the same is vital as they affect the overall physical, chemical, and mechanical properties [25]. However, such determinations in steel have not been part of the study so far. For example, in material science, scanning probe microscopy has revealed point defects in h-BN but has not enabled accurate classification [26]. On the other hand, secondary ion mass spectrometry revealed high C and O content; however, it does not distinguish the local bonding [27]. Whereas transmission electron microscopy differentiated V_B and V_N; however, beam damage is often inevitable [28]. While microscopy has been employed to investigate defects in h-BN, complementary methods providing element-specific bonding information are required. X-PEEM spectro-microscopic equipped with XAS, an element-specific technique, can provide local bonding and structural information sensitive to perturbations caused by defects. As per the literature and the formation energies of selected defect structures, the most favorable passivated point vacancy is the V_N. Furthermore, the formation energies of the point vacancies are lowered after C and O substitution, showing that vacancy filling is energetically favorable. Although the formation energy of C_B defect is lower than C_N theoretically [18], we have observed C_N in the studied inclusions. O contamination is difficult to eliminate and is, thus, responsible for the additional features observed. The observation of O_N defects is supported by the fact that the O_N has lower formation energy than O_B. As per calculations, O_N is the most favorable substitutional defect, implying any V_N would fill with O if available, which is consistent with the in-situ XAS presented here. In addition, it has been proposed that the formation energies of defect structures containing two or three O atoms substituting N sites: O_{2N} and O_{3N}, respectively, are high and are proposed to be energetically unfavorable compared with O_N. Nevertheless, these are observable experimentally, as noted herein and in the literature [21,22]. Moreover, the shape and energy positions of spectral features A-C agree with the simulation carried out by Huber et al. [21] and, thus, confirms the formation of $BN_{3-x}O_x$ ($1 \leq x \leq 3$) O defects in h-BN. Thus, O exposure leads to partial substitution of N atoms and hence to the three possible local oxide configurations BN_2O (A), BNO_2 (B), and BO_3 (C) as shown in Fig. 7. The dominance of O-terminated defects can be attributed to enough O present during the steel-making process.

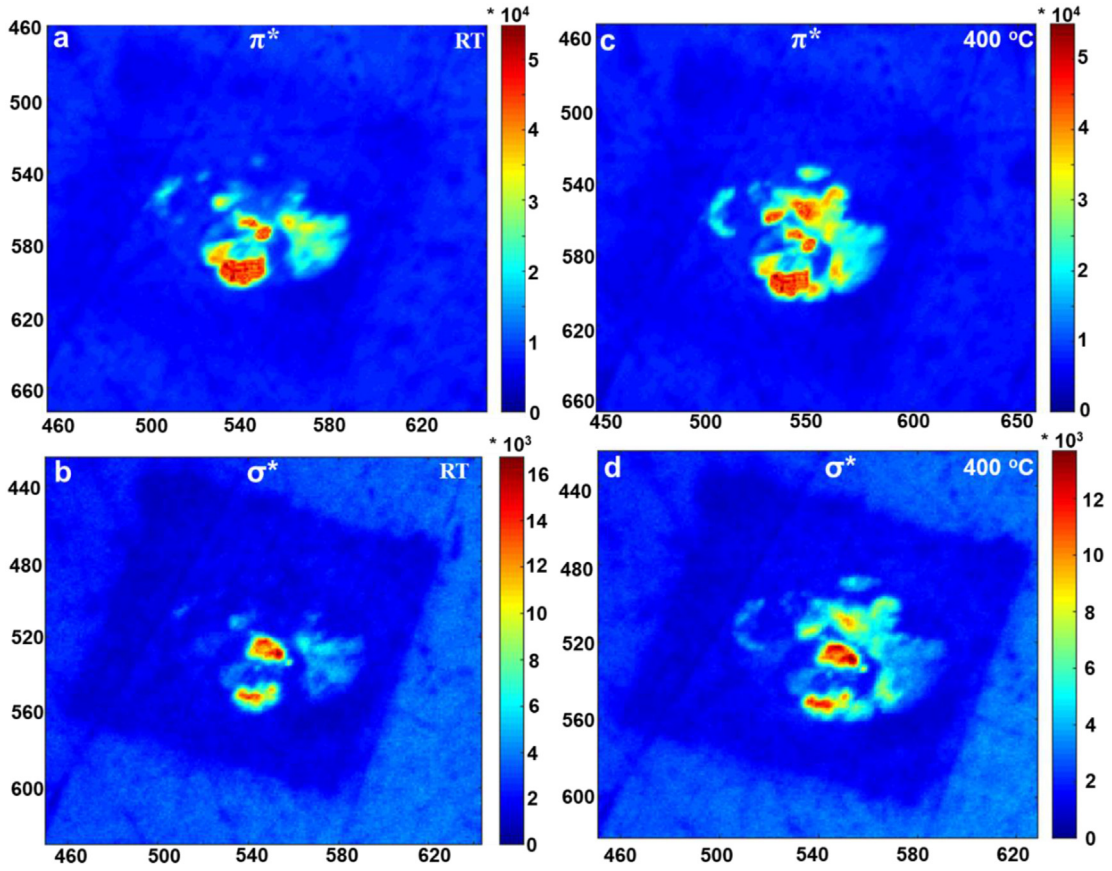

Fig. 6 – False color distribution maps displaying the maximum energy absorption in the local spatial variation in the 200 × 200 pixels field of view for inclusion A2 at RT (a & b) and 400 °C (c & d), Top to bottom, pixels colored with the intensity (number of counts) shown at one pixel as a function of energy. Contrast and quantitative image analysis were distributed between blue color (lowest absorption) and red (highest absorption).

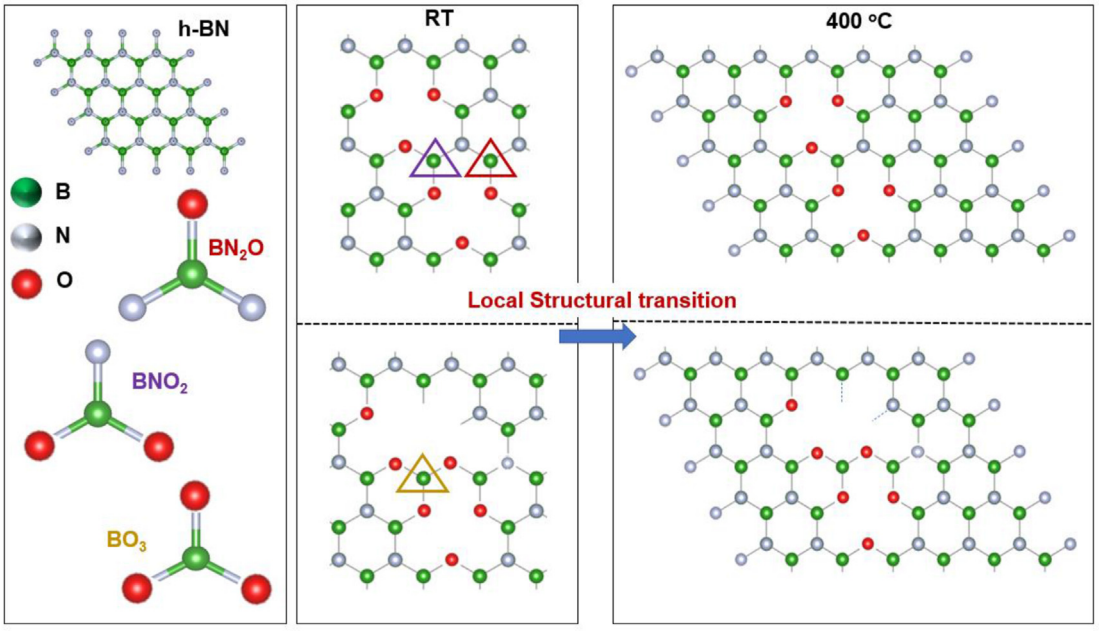

Fig. 7 – Schematic representation of local structural changes in h-BN during vacuum annealing at 400 °C. Defect structures in a h-BN host crystal with different defects, while maintaining twofold coordination for the O atoms and threefold coordination for N and B atoms. The color of the triangles around selected boron atoms correspond to BN_2O, BNO_2, and BO_3 environments.

4.2. *Adjusting nature of h-BN, a temperature effect*

Although the detailed formation mechanism of NMI is critical, knowledge of the temperature-induced local structural changes is also essential when considering the investigation of various processing conditions on macroscopic properties of the complex steel system. Despite continuous advancement in in-house and synchrotron methods, there is a scarcity of either experimental techniques or research infrastructure for materials wherein the response to the external stimulation such as high temperature is weak and complex [29]. Hence, the challenge is to measure these changes non-destructively. This is also because the time-dependence of a material system to an external effect on atomic and micron length scales vary and has been a key to understanding many physical and chemical properties, especially when materials exhibit a dynamic response to external perturbation, such as temperature, pressure, and electric field. For instance, in a recently discovered non-classical electrostrictors (e.g., 10% Gd doped CeO_2) with only *ca*. 10% of Ce ions located near O ion vacancies respond to the modulations of the external electric field and contribute to the observed giant electrostriction [30]. Furthermore, changes in local coordination around the B atom due to change in surrounding environments due to an external stimulus of high pressure [31] and gas composition [32] have been investigated. In the current scenario, vacuum annealing at 400 °C has led to a decrement in defects (Fig. 7) followed by BN adjustment and possibly other phases within A1 and A2 inclusions. This study implies that conditions at tempering stage can manipulate various NMIs in the steel matrix along with varied interfacial interaction between inclusions and steel matrix, which needs to be probed to control inclusion formation towards clean steel production.

5. Summary and conclusion

In summary, the results presented in this work depict manipulation and monitoring of the local spectro-microscopic behavior of chosen BN inclusion embedded within ultra-high-strength steel via X-ray absorption (XAS)-photoelectron emission microscopy (X-PEEM). X-PEEM investigation on two different inclusions (A1 and A2) suggests the formation of h-BN inclusion, although scanning electron microscopy-energy dispersive spectroscopy (SEM-EDS) did not give reliable evidence of boron in inclusion. This observation emphasizes the application of sensitive and highly selective spectro-microscopic methods to probe complex NMIs. Noted variation in the relative intensity of π^*/σ^* excitonic peaks in room temperature XAS spectra at spatially different locations is assigned to polarization and or thickness effects. Furthermore, the occurrence of multiple minute features above the π^* peak in the energy range of 192–195 eV are ascribed to single, double, or triple O substituted N defects ($O_{N,2N,3N}$), which are more dominant in A2 inclusion. The detected weak shoulder on the left side of π^* peak in both the room and high-temperature XAS spectra is ascribed to the interaction between h-BN inclusion with Ca-based inclusion and or steel matrix. Significant changes in the high-temperature B K-edge XAS spectra such as relative intensity of π^*/σ^* excitonic peaks at the same location and reduced intensity of defects suggest the adjusting nature of BN inclusion with the implication of external stimulus of temperature, a commonly used practice to enhance the steel's performance. Addition of boron is expected to improve steel hardenability, provided boron is evenly dissolved in the matrix. Though the TiN formation has alleviated the nitridation of boron into BN inclusions, the existence of the micrometer-sized inclusions again affects overall materials performances. The presented results show that relatively low temperatures, comparable to tempering stage, can affect chemical states of the micrometer-sized inclusions as well. As a result, the heat treatment at different temperatures shall be considered to alter the formation of the nitride inclusions and even smaller particles, such as precipitates. While the former may impact the mechanical properties, the latter may also be beneficial thanks to precipitation hardening. The present spectro-microscopic elucidation of the behavior of BN inclusion during conditions comparable to tempering stage offers the possible engineering route that are beyond understanding formation mechanism of BN inclusion within steel matrix.

Declaration of Competing Interest

The authors declare no competing interests.

Acknowledgment

Authors acknowledge Academy of Finland grant #311934 and Kvantum Institute, University of Oulu (Project CLEAN2STEEL) for the financial support. We also thank the crew of the MAX IV laboratory for their support during the beamtime operation. Authors would like to thank Mr. Tun Nyo for the assistance in sample preparation for SEM and X-PEEM, Mr. Jaakko Hannula for insightful discussions, and the Centre for Material Analysis, University of Oulu is also acknowledged for in-house characterizations.

Appendix A. Supplementary data

Supplementary data to this article can be found online at https://doi.org/10.1016/j.jmrt.2022.01.170.

REFERENCES

[1] Zhou T, Xiong Y, Yue Y, Lu Y, Chen Y, He T, et al. Controlled cold rolling effect on microstructure and mechanical properties of Ce-modified SAF 2507 super duplex stainless steel. Mater Sci Eng, A 2019;766:138352. https://doi.org/10.1016/j.msea.2019.138352.

[2] Zhou T, Xiong Y, Zha X, Yue Y, Lu Y, He T, et al. Hot-deformation-induced structural and mechanical properties of Ce-modified SAF 2507 super duplex stainless steel. J Mater

Res Technol 2020;9:8379–90. https://doi.org/10.1016/j.jmrt.2020.05.123.
[3] Da Costa E Silva ALV. The effects of non-metallic inclusions on properties relevant to the performance of steel in structural and mechanical applications. J Mater Res Technol 2019;8:2408–22. https://doi.org/10.1016/j.jmrt.2019.01.009.
[4] Holappa L, Wijk O. Inclusion engineering. 1st ed., vol. 3. Elsevier; 2014. https://doi.org/10.1016/B978-0-08-096988-6.00008-0.
[5] Burja J, Koležnik M, Župerl Š, Klančnik G. Nitrogen and nitride non-metallic inclusions in steel. Mater Tehnol 2019;53:919–28. https://doi.org/10.17222/mit.2019.247.
[6] Suito H, Inoue R. Thermodynamics on control of inclusions composition in ultra-clean steels. ISIJ Int 1996;36:528–36. https://doi.org/10.2355/isijinternational.36.528.
[7] Jung IH, Decterov SA, Pelton AD. Computer applications of thermodynamic databases to inclusion engineering. ISIJ Int 2004;44:527–36. https://doi.org/10.2355/isijinternational.44.527.
[8] Imashuku S, Wagatsuma K. Cathodoluminescence analysis of nonmetallic inclusions of nitrides in steel. Surf Interface Anal 2019;51:31–4. https://doi.org/10.1002/sia.6539.
[9] Bandi B, Santillana B, Tiekink W, Koura N, Williams M, Srirangam P. 2D automated SEM and 3D X-ray computed tomography study on inclusion analysis of steels. Ironmak Steelmak 2020;47:47–50. https://doi.org/10.1080/03019233.2019.1652437.
[10] Janis D, Inoue R, Karasev A, Jönsson PG. Application of different extraction methods for investigation of nonmetallic inclusions and clusters in steels and alloys. Adv Mater Sci Eng 2014;2014:1–8. https://doi.org/10.1155/2014/210486.
[11] Rani E, Ingale AA, Chaturvedi A, Kamal C, Phase DM, Joshi MP, et al. Correlation of size and oxygen bonding at the interface of Si nanocrystal in Si-SiO2 nanocomposite: a Raman mapping study. J Raman Spectrosc 2016;47:457–67. https://doi.org/10.1002/jrs.4832.
[12] Shi X, Posysaev S, Huttula M, Pankratov V, Hoszowska J, Dousse JC, et al. Metallic contact between MoS2 and Ni via Au nanoglue. Small 2018;14:1–10. https://doi.org/10.1002/smll.201704526.
[13] Singh H, Alatarvas T, Kistanov AA, Aravindh SA, Wang S, Zhu L, et al. Unveiling interactions of non-metallic inclusions within advanced ultra-high-strength steel: a spectro-microscopic determination and first-principles elucidation. Scripta Mater 2021;197:113791. https://doi.org/10.1016/j.scriptamat.2021.113791.
[14] Cao W, Pankratov V, Huttula M, Shirmane L, Niu YR, Wang F. X-ray photoemission electron microscope determination of origins of room temperature ferromagnetism and photoluminescence in high co-content Co xZn1-xO films. Surf Rev Lett 2014;21:1–11. https://doi.org/10.1142/S0218625X14500589.
[15] Shi X, Huttula M, Pankratov V, Hoszowska J, Dousse J-C, Zeeshan F, et al. Quantification of bonded Ni atoms for M-M0S2 metallic contact through X-ray photoemission electron microscopy. Microsc Microanal 2018;24:458–9. https://doi.org/10.1017/s1431927618014526.
[16] Wang J, Wang Z, Cho H, Kim MJ, Sham TK, Sun X. Layer speciation and electronic structure investigation of freestanding hexagonal boron nitride nanosheets. Nanoscale 2015;7:1718–24. https://doi.org/10.1039/c4nr04445b.
[17] Ohtomo M, Yamauchi Y, Sun X, Kuzubov AA, Mikhaleva NS, Avramov PV, et al. Direct observation of site-selective hydrogenation and spin-polarization in hydrogenated hexagonal boron nitride on Ni(111). Nanoscale 2017;9:2369–75. https://doi.org/10.1039/c6nr06308j.
[18] McDougall NL, Partridge JG, Nicholls RJ, Russo SP, McCulloch DG. Influence of point defects on the near edge structure of hexagonal boron nitride. Phys Rev B 2017;96:1–9. https://doi.org/10.1103/PhysRevB.96.144106.
[19] Ma H, Lin SH, Carpenter RW, Rice P, Sankey OF. Ab initio calculation of band structure, x-ray emission, quantum yield, and electron-energy-loss spectra of hexagonal boron nitride. J Appl Phys 1993;73:7422–6. https://doi.org/10.1063/1.353983.
[20] Peter R, Bozanic A, Petravic M, Chen Y, Fan LJ, Yang YW. Formation of defects in boron nitride by low energy ion bombardment. J Appl Phys 2009;106. https://doi.org/10.1063/1.3253576.
[21] Huber SP, Gullikson E, Van De Kruijs RWE, Bijkerk F, Prendergast D. Oxygen-stabilized triangular defects in hexagonal boron nitride. Phys Rev B Condens Matter 2015;92:1–7. https://doi.org/10.1103/PhysRevB.92.245310.
[22] Makarova AA, Fernandez L, Usachov DY, Fedorov A, Bokai KA, Smirnov DA, et al. Oxygen intercalation and oxidation of atomically thin h-BN grown on a curved Ni crystal. J Phys Chem C 2019;123:593–602. https://doi.org/10.1021/acs.jpcc.8b10574.
[23] Fernandez L, Makarova AA, Laubschat C, Vyalikh DV, Usachov DY, Ortega JE, et al. Boron nitride monolayer growth on vicinal Ni(1 1 1) surfaces systematically studied with a curved crystal. 2D Mater 2019;6. https://doi.org/10.1088/2053-1583/ab01e7.
[24] Khare S. Approximations in using solubility products for B, N, Ti and Al. Mater Sci Technol 2011;27:1863–8. https://doi.org/10.1179/026708309X12512744154126.
[25] Jang SK, Youn J, Song YJ, Lee S. Synthesis and characterization of hexagonal boron nitride as a gate dielectric. Sci Rep 2016;6:8583–90. https://doi.org/10.1038/srep30449.
[26] Wong D, Velasco J, Ju L, Lee J, Kahn S, Tsai HZ, et al. Characterization and manipulation of individual defects in insulating hexagonal boron nitride using scanning tunnelling microscopy. Nat Nanotechnol 2015;10:949–53. https://doi.org/10.1038/nnano.2015.188.
[27] Taniguchi T, Watanabe K. Synthesis of high-purity boron nitride single crystals under high pressure by using Ba-BN solvent. J Cryst Growth 2007;303:525–9. https://doi.org/10.1016/j.jcrysgro.2006.12.061.
[28] Meyer JC, Chuvilin A, Algara-Siller G, Biskupek J, Kaiser U. Selective sputtering and atomic resolution imaging of atomically thin boron nitride membranes. Nano Lett 2009;9:2683–9. https://doi.org/10.1021/nl9011497.
[29] Singh H, Donetsky D, Liu J, Attenkofer K, Cheng B, Trelewicz JR, et al. Investigation of periodically driven systems by x-ray absorption spectroscopy using asynchronous data collection mode. Rev Sci Instrum 2018;89. https://doi.org/10.1063/1.5000679.
[30] Korobko R, Patlolla A, Kossoy A, Wachtel E, Tuller HL, Frenkel AI, et al. Giant electrostriction in Gd-doped ceria. Adv Mater 2012;24:5857–61. https://doi.org/10.1002/adma.201202270.
[31] Lee SK, Eng PJ, Mao HK, Meng Y, Newville M, Hu MY, et al. Probing of bonding changes in B2O3 glasses at high pressure with inelastic X-ray scattering. Nat Mater 2005;4:851–4. https://doi.org/10.1038/nmat1511.
[32] Love AM, Thomas B, Specht SE, Hanrahan MP, Venegas JM, Burt SP, et al. Probing the transformation of boron nitride catalysts under oxidative dehydrogenation conditions. J Am Chem Soc 2019;141:182–90. https://doi.org/10.1021/jacs.8b08165.